

Accuracy of super-resolution for hyperspectral ocean observations

Joseph L Garrett, Dennis Langer, Karine Avagian, and Annette Stahl

Norwegian University of Science and Technology, 7034 Trondheim, Norway

Abstract—Super-resolution, a class of techniques used to reconstruct a high-resolution image from one or more low-resolution observations, is a possible route to utilize the full remote imaging capabilities of small satellites and unmanned aerial vehicles. Here, we test two frequently-used variants, Robust Super-Resolution (RSR) and Projection onto Convex Sets (POCS), to see how accurately each technique reconstructs images from a small satellite. The two techniques are chosen because each utilizes a different kind of prior knowledge. RSR utilizes knowledge about the scene, while POCS utilizes knowledge about the imaging process. The algorithms are run on three bands of two hyperspectral images: one lab-acquired image of a wooden block and one simulated image of a remote sensing ocean scene. The super-resolution reconstructions of the simulated image are evaluated by calculating the brightness error and spectral angle with respect to the original scene. Both super-resolution algorithms improve both metrics relative to the raw, registered data. RSR achieves more improvement overall, but POCS operates faster.

I. INTRODUCTION

When ocean phenomena such as algae blooms occur, it is critical to monitor them with a high temporal, spatial, and spectral resolution, both to study their population dynamics for oceanographic purposes and to ensure quick warning to any aquaculture sites in the path of the bloom [1]. Small mobile platforms such as cubesats and unmanned aerial vehicles are ideal to achieve high temporal resolution because they offer the opportunity for decentralized and rapid oceanic remote sensing [2], [3] (figure 1). Hyperspectral imagers (HSIs)

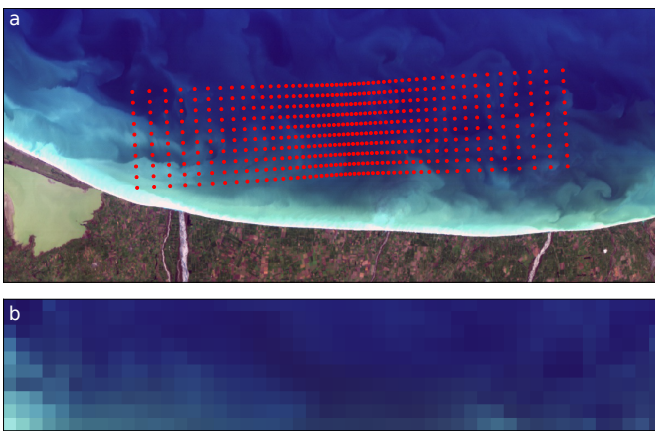


Fig. 1. The coastline near Te Waihora, New Zealand imaged by the Hyperspectral Imager of the Coastal Ocean (HICOTM) on June 16, 2011 with the centers of the pixels of our simulated image indicated as red points (a). The measurements, before registration, from the imaging simulation (b). The red, green, and blue bands are at 639, 553 and 461 nm, respectively.

enable imaging of the ocean with high spectral resolution (< 10 nm) [4], [5]. However, the spatial resolution of HSIs that can fit on small platforms is limited.

Super-resolution techniques are a way to combine spatially-separated low resolution observations to reconstruct a higher-resolution image [6], [7]. They are one possible way of enhancing the low spatial resolution of HSIs ocean images. Many super-resolution algorithms are developed for specific scenarios, such as resolving text, in which there are sharp boundaries between distinct regions of the image [8]. However, the shapes of features in the ocean are often not known beforehand, and the sharp boundaries of land are replaced by smoother gradients. Therefore, super-resolution algorithms may perform significantly differently on images of the ocean than on text or other human-scale scenes.

Here we evaluate the accuracy of two super-resolution algorithms by comparing their reconstructions to a higher-resolution RGB image to determine their reliability for ocean science. The methods used to adapt super-resolution algorithms from monochromatic images to RGB images can be scaled for HSI images. Using RGB images simplifies the problem for these initial tests. The two methods are: projection onto convex sets (POCS) [9] and the robust super resolution (RSR) of Farsiu *et al.* [8]. RSR is an optimization-based technique that maximizes a statistical property of the reconstruction, typically smoothness. Instead, POCS adjusts the reconstruction to make it consistent with the measurements while considering the measurement procedure pointwise. These two algorithms permit the comparison of how different kinds of prior knowledge, such as about the imaged scene (RSR) or about the imaging process (POCS) affects the accuracy of super-resolution reconstruction. Earlier studies found that, for human-scale and microscopic images, the prior knowledge about the scene is more important than knowledge about the imaging process [10], [11], but that may differ for ocean scenes, which have smoother boundaries. The implementations of the two algorithms used here are described in more mathematical detail below.

The super-resolution algorithms are tested on an image acquired in the lab and a simulated image. A traditional test sample for super-resolution algorithms contains many sharp boundaries, such as text, in which recognizable characters are used to signify reconstruction validity. Because the features of interest in oceanic remote sensing are often have smooth rather than sharp boundaries, we choose to image a block of wood that has both sharp edges and a smoother texture to the wood itself (figure 2). It is imaged from about 3 meters away using a

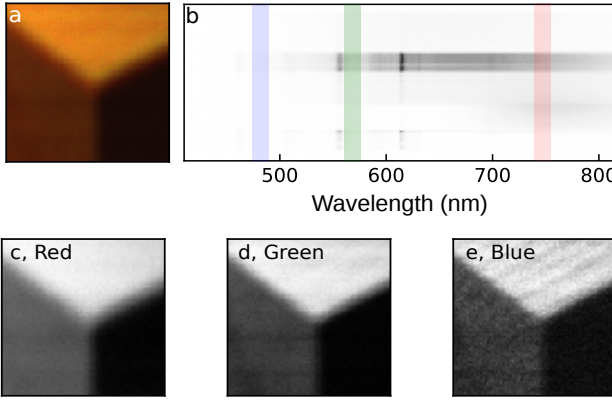


Fig. 2. A block of wood is used as a test hyperspectral scene (a) because it contains both sharp edges and smooth textures. The red, green, and blue bands are depicted on the spectrum (b). The different bands show different amounts of texture (c-e).

version of the hyperspectral camera described in [5]. Because the image does not have a ground truth, the reconstructions of the wood image are evaluated only qualitatively.

In the following, we first discuss the measurement model which is both used as the method for simulating the image acquisition and as the description of imaging process in the lab experiment. A simple way of reversing the imaging process is then described and used to perform image registration. Next, the metrics used to evaluate the accuracy of reconstructions are introduced. The super-resolution techniques are described before being applied to the test images. Then the results of the tests are discussed and the two techniques are compared. Finally, we conclude with a discussion of the feasibility of super-resolution for remote sensing of the ocean and identify questions that must be answered before super-resolution can be reliably incorporated into an ocean science data pipeline.

II. IMAGING AND IMAGE REGISTRATION

The mathematical description of the imager used for the simulations is similar to earlier works [8], [7], but has been abstracted slightly because the push-broom design implies that pixels are captured sequentially by a line scanner, similar to a rolling shutter design, rather than an array of pixels

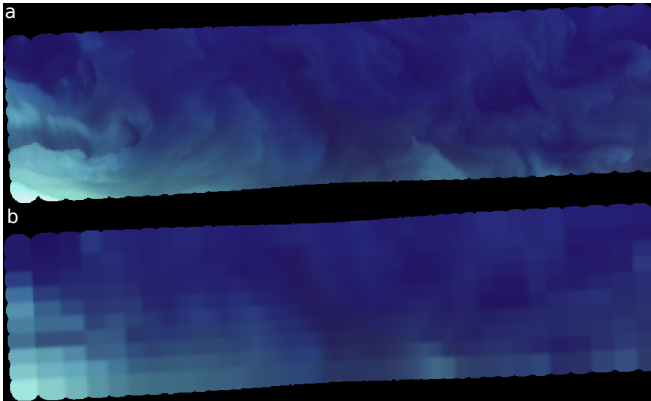


Fig. 3. The HICO™ scene on the registered image grid (a). The registered measurements (b).

[12], [13]. However, we ignore all issues related to depth because the entire scene is essentially at the same distance from the camera. In addition, we model imaging during a slew maneuver in order to maximize the amount of time that the camera points towards the target location. Because of this, the low-resolution observations used in the reconstruction do not image locations on a spatial grid (figure 1b). Therefore, the basic relationship between the scene and the measurements is written as:

$$\underline{Y} = \mathbf{M}\underline{X}, \quad (1)$$

where \underline{Y} is an $n_{\text{meas}} \times n_{\text{bands}}$ matrix of measurements, \underline{X} is an $n_{\text{pix}} \times n_{\text{bands}}$ matrix of the pixels in the scene, and \mathbf{M} is an $n_{\text{meas}} \times n_{\text{pix}}$ matrix that describes how each measurement originates from the scene. The matrices \underline{Y} and \underline{X} are non-negative, and, so long as the pixel footprint function is non-negative, \mathbf{M} is non-negative as well. Moreover, if \underline{Y} and \underline{X} are similarly normalized, then \mathbf{M} has the property that:

$$\sum_{j=1}^{n_{\text{pix}}} M_{ij} = 1, \quad (2)$$

for each row i . For most realistic hyperspectral imagers, the pixel footprint function varies with wavelength [14]. In that case, equation 1 may be generalized so that \mathbf{M} is different for each wavelength of light. Note that this framework can incorporate additional measurements simply by appending the additional measurements to the bottom of \underline{Y} and appending a row to the bottom of \mathbf{M} , so long as the pixel footprint of the additional measurement is at least as large as the pixels in \underline{X} . Below, several different collections of matrices that satisfy equation 1 are used, and they are distinguished by subscripts.

In the simulations, a matrix to describe the simulated imaging process, \mathbf{M}_{sim} , is calculated from the simulated trajectory of a satellite carrying a camera pointed at the earth [15] and the pixel footprint function of the camera. In the experiment, it is calculated using a pixel footprint function estimated from the images themselves. The simulated measurement of the scene, $\underline{Y}_{\text{meas}}$, is calculated as: $\underline{Y}_{\text{meas}} = \mathbf{M}_{\text{sim}}\underline{X}_{\text{HICO}}$, where $\underline{X}_{\text{HICO}}$ is the HICO™ scene.

Image registration, the placing of information from measured data on a predetermined grid, is critical for both remote sensing and super-resolution techniques (figure 3). Here, we perform image registration based on \mathbf{M}_{sim} . First, we define a new sub-selected matrix, \mathbf{M}_{sub} from \mathbf{M}_{sim} removing the columns that represent pixels which contribute less than $10^{-4}\%$ of the signal. Second, the rows are normalized so that equation 2 remains satisfied. Then the remaining columns each correspond to a pixel in the original image. A blank registered image is prepared by choosing the smallest rectangle which encloses all the pixels which correspond to the remaining columns. A mask is used to indicate which pixels in the registered image contribute the measurement. Up to the threshold used to select for \mathbf{M}_{sub} , the spatial pixels in the registered region are still $\underline{Y}_{\text{meas}} = \mathbf{M}_{\text{sub}}\underline{X}_{\text{sub}}$, where $\underline{X}_{\text{sub}}$ is the portion of the scene from when the measurements originate.

Finally, the spectra to assign to each pixel are identified by reversing the imaging process described by \mathbf{M}_{sub} . We suppose

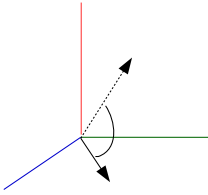


Fig. 4. The spectral angle between two pixels, each represented by a vector in RGB-space.

both that the spectra at a particular pixel should be a linear combination of the spectra the measurements that it contributes to and that the weight of the contribution of each measurement to the pixel then should be proportional to its contribution to a measurement, to some power. An example of a matrix which describes such a process is $\tilde{\mathbf{M}}_{\text{sub}}$:

$$\tilde{M}_{ij} = \frac{(M_{ji})^q}{\sum_{k=1}^{n_{\text{meas}}} (M_{ki})^q}, \quad (3)$$

where M_{ji} are the elements of the \mathbf{M}_{sub} , q is a parameter that can vary between 0 and infinity. The matrix with $q = 1$ is used here because it causes each registered pixel to be a linear combination of the measurement spectra in the same proportions in which the region represented by the pixel contributes to the measurements. If all the measurements have the same Gaussian pixel footprint function, the $q = 1$ case is approximately equivalent to inverse distance weighted interpolation, which is discussed in [13], whereas $q \gg 1$ would be nearest-neighbor interpolation and $q = 0$ would attribute the average spectra of all the measurements to each pixel. Then the registered image is:

$$X_{\text{reg}} = \tilde{\mathbf{M}}_{\text{sub}} Y_{\text{meas}}. \quad (4)$$

The grid of the original scene is maintained for the registration in order to ease the evaluation of the accuracy of the reconstruction algorithms. However, any grid over the imaged location could be chosen by this method.

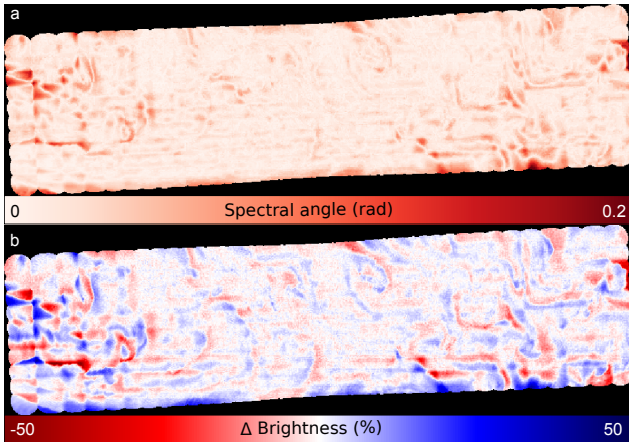


Fig. 5. The spectral angle between the scene and the registered image (a). The difference in brightness between the scene and registered image (b).

III. EVALUATING ACCURACY

We use two metrics to evaluate the accuracy of the super-resolution reconstructions (figures 4 and 5). The key quantity that distinguishes hyperspectral images from is spectral information. Therefore, the primary metric we use to evaluate the reconstructions is the spectral angle, which quantifies the difference between the spectra of the original and reconstructed pixels:

$$\theta(\vec{x}_i, \vec{x}_j) \equiv \cos^{-1} \left(\frac{|\vec{x}_i| |\vec{x}_j|}{|\vec{x}_i \cdot \vec{x}_j|^2} \right), \quad (5)$$

where \vec{x}_i is the spectrum of a pixel as a vector in an $\mathbb{R}^{n_{\text{bands}}}$ space. The second metric we use is the brightness error:

$$e_b(\vec{x}_i, \vec{x}_j) \equiv |\vec{x}_i| - |\vec{x}_j|. \quad (6)$$

It is used, rather than the more common band-wise mean squared error, because it shows spatially whether the reconstruction overestimates or underestimates the image and, in our preliminary tests, seemed to be less correlated with the spectral angle. When it is reported as a single number, the mean absolute value is reported. Moreover, both spectral angle and brightness error are not quantities that are directly operated on by any of the super-resolution techniques, so they are plausibly unbiased proxies of the image quality.

In order to understand how super-resolution algorithms affect the reliability of ocean observations, the error metrics are investigated for groups of individual pixels. To sort the pixels, we define two quantities: contribution and isolation (figure 6). The contribution is defined as how much a pixel contributes to all the measurements:

$$\chi(p_j) = \sum_{i=1}^{n_{\text{meas}}} M_{ij}, \quad (7)$$

where the M_{ij} are the elements of the matrix \mathbf{M}_{sub} . Similarly, the isolation is the proportion of χ_j which comes from one element:

$$\eta(p_j) = \frac{\max_i(M_{ij})}{\chi(p_j)}, \quad (8)$$

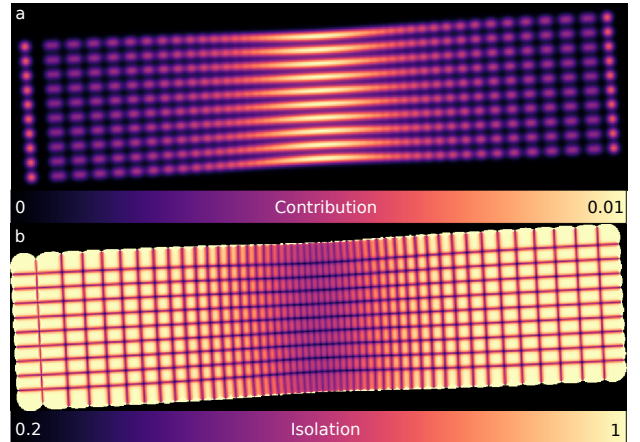


Fig. 6. The summed contributions of each pixel to the measurements (a). The isolation of each pixel (b).

where $\max_i(M_{ij})$ indicates the largest element of the j th column, and p_j is the j th pixel in the image. These two ways of sorting the pixels are coupled, but below it is shown that they illuminate rather different aspects of the super resolution algorithms.

IV. DESCRIPTION OF TECHNIQUES

In first super-resolution algorithm tested, robust super-resolution (RSR), the procedure is split into an image reg-

istration component and a smoothing component [8]. Here, because the same image registration technique is used for both algorithms, we focus on the smoothing component. RSR is a optimization-based technique in which a cost function, based on both the consistency with the data and the smoothness of the reconstruction, is minimized by gradient descent. It is thus possible to consider RSR as a type of Bayesian maximum a posteriori algorithm in which the smoothness term is the prior knowledge about the scene. The cost function then takes the form:

$$E = E_{\text{cons}} + \lambda E_{\text{smth}}. \quad (9)$$

The primary innovation of RSR is then its choice to use the L_1 - rather than the L_2 -norm for E_{cons} and E_{smth} . A class of bilateral filters is introduced by [8] to improve the speed of the algorithm, as they can be written in terms of shifts along the horizontal and vertical axes. The terms for the L_1 -norm reconstruction are then :

$$E_{\text{cons}} = \|\mathbf{M}_{\text{sub}} \underline{X}_{\text{rec}} - \underline{Y}\|_1, \quad (10a)$$

$$E_{\text{smth}} = \sum_{l=-2}^2 \sum_{m=\max(0,-l)}^2 \|\underline{X}_{\text{rec}} - S_x^l S_y^m \underline{X}_{\text{rec}}\|_1, \quad (10b)$$

where the S_x^l indicates a shift by l pixels along the x -axis. Gradient descent is used to minimize E , so the updated reconstructions are:

$$\underline{X}_{\text{rec}}^{n+1} = \underline{X}_{\text{rec}}^n - \beta \nabla E(\underline{X}_{\text{rec}}^n), \quad (11)$$

where β is a parameter used to determine the rate of descent along the gradient, $\underline{X}_{\text{rec}}^n$ is the n th reconstruction (starting with $n = 0$ as the registered image).

Instead of focusing on assumptions about the smoothness of the scene, the second algorithm emphasizes knowledge about the imaging process [9]. Projection on to convex sets (POCS) posits that there is a subset of the set of all possible images that is consistent with the measurements. The subset is convex because any linear combination of reconstructions from the set is also a member of the set. In POCS, projection operators are iteratively applied to make the reconstruction consistent with each measurement. Another constraint, non-negativity, is also incorporated. It is similar to the iterative back projection technique [16], but the more general projection operator makes it more versatile [6]. Although noise can harm the POSC algorithm, we do not compensate for it directly here, but there are methods to do so [17], [18].

There is considerable freedom in how a reconstruction can be projected onto the measurement-consistent set, and here we choose a projection that permits control over the frequencies used in the reconstruction. A projection operator acting on measurement i , P_i , should make $\epsilon_i = (\mathbf{M}_{\text{sub}} \underline{X}_{\text{rec}} - \underline{Y}_{\text{meas}})_i$ vanish, or at least approach the noise level, where $\underline{X}_{\text{rec}}^{n+1} = P_i(\underline{X}_{\text{rec}}^n)$. Here we choose a class of projection operators:

$$P_{i,q}(\underline{X}, \epsilon_i) = \underline{X} - \frac{\tilde{\mathbf{M}}(q)_i}{(\mathbf{M}_{\text{sub}} \tilde{\mathbf{M}}(q))_{ii}} \epsilon_i, \quad (12)$$

where $(\mathbf{M}_{\text{sub}} \tilde{\mathbf{M}}(q))_{ii}$ denotes the i th diagonal element of the matrix $(n_{\text{meas}} \times n_{\text{meas}})$ and $\tilde{\mathbf{M}}(q)_i$ denotes the i th column

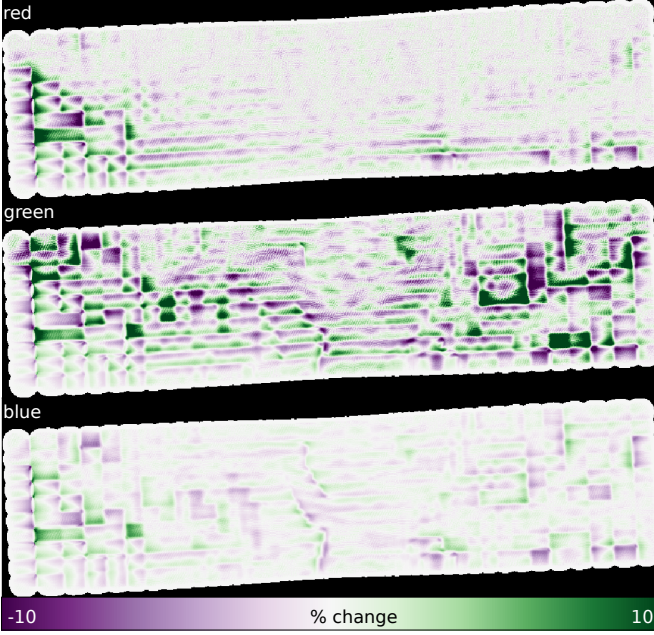


Fig. 7. The change in the red, green, and blue bands relative to the registered image when the robust super resolution with L_1 -norm data consistency and bilateral regularization are applied (equation 10).

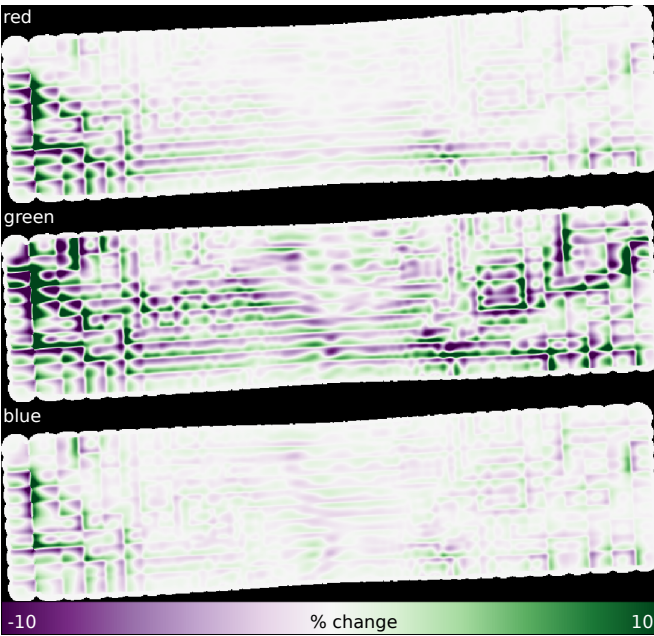


Fig. 8. The change in the red, green, and blue bands relative to the registered image when the robust super resolution with L_2 -norm data consistency and bilateral regularization are applied.

of $\tilde{\mathbf{M}}(q)$ (length n_{pix} , equation 3). In the case $q = 1$, this reduces to a common POCS projection operator [6]. Shifting q to a lower value corresponds to performing POCS with lower frequencies. The element-wise non-negativity projection, $P_{\geq 0}(\underline{X}) = \max(0, \underline{X})$, is also used. To run the algorithm, the pixels are randomly ordered and the $P_{i,q}$ projections are applied sequentially. Once the $P_{i,q}$ projections have been applied to each pixel, $P_{\geq 0}$ is applied to the whole image. The two-step procedure is then repeated for a specified time.

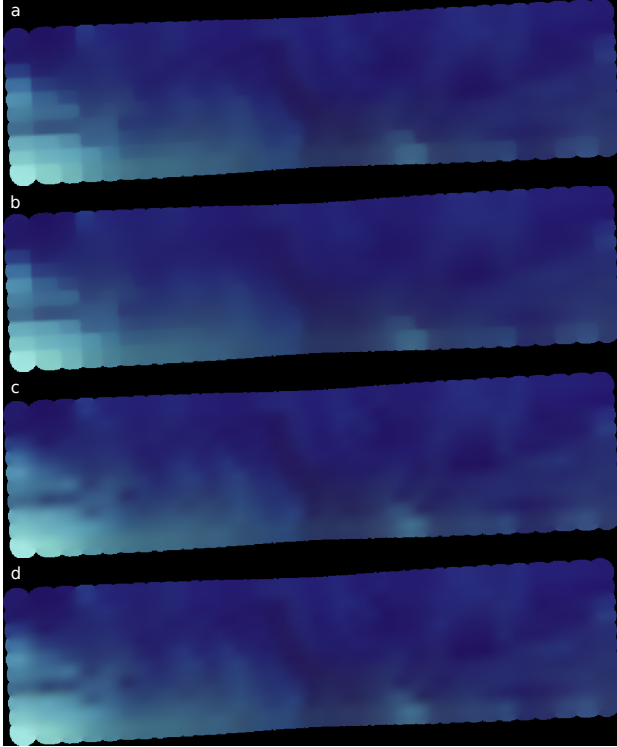


Fig. 9. The RGB reconstructions from the RSR algorithms using the L1-norm for both data consistency and smoothness (a), the L2-norm for data consistency and the L1-norm for smoothness (b), the L2-norm for both data consistency and smoothness (c), and the L2-norm for both data consistency and smoothness plus an extra color-consistency term (d).

V. EXPERIMENTS

Both super-resolution techniques are evaluated by using them to reconstruct the ocean scene from the simulated measurement data. The results for both algorithms are summarized in table I. The settings that achieve the best metrics with each algorithm are highlighted.

The RSR algorithm is tested on the simulated ocean scene with five different cost functions. All the tests are standardized by being given 6 minutes to run, so that it is possible to see how the metrics of the resulting reconstructions evolve in time. First, the L_1 -norm is used for both data consistency and smoothness, according to equation 10, with $\beta = 10$ and $\lambda = 0.01$. The λ and β are chosen by running the algorithm several times and selecting the maximum values which give a stable image. The green channel changes the most relative to the registered image, and some high-frequency noise has appeared (figure 7). Next, the L_2 -norm is used

for both data consistency and L_1 -norm for smoothness, after adapting equation 10 to use the L_2 -norm where appropriate. When L_1 -norm is used for both data consistency and L_2 -norm for smoothness, and when L_2 -norm is used everywhere, $\lambda = 0.005$ (figure 8). Finally, a third energy term that couples the different colors is added to the equation 9 [19]. Four of the five reconstructed images are shown in figure 9. The algorithm is also tested on the wooden block (figure 10) and shows that the both regularization terms help to prevent the high-frequency noise that occurs when only the data-consistency term is used. All five reconstructions of the simulated data improve the brightness error, and four of five improve the spectral angle (table I). In general, the RSR algorithm that shows some improvement for most χ , and actually improves more for larger η (figure 11).

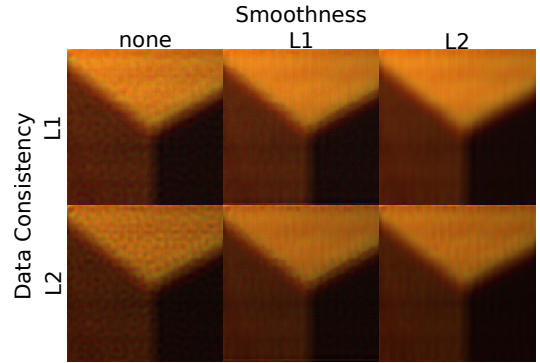


Fig. 10. Image of the wooden block after operated on by the RSR algorithm with both L_1 - and L_2 -norms.

The POCS algorithm is tested with varying values of q to understand how the frequencies used affect the reconstruction. POCS reconstructs the simulated ocean observations with $q = 0.5$ or 1.0 (figures 12 and 13). Both reconstructions improve both the spectral angle and the brightness error relative to the raw registered image, although $q = 0.5$ performed better on both metrics. Note that because the values in \mathbf{M}_{sub} are truncated to 10^{-7} , values of q below 0.5 leave circle-shaped artifacts in the final image. The artifacts can be reduced by truncating at a smaller value, but doing so would make \mathbf{M}_{sub} more dense and thus greatly expand the computational time required. Running POCS with q ranging from 0.2 to 2 (figure 14) shows that decreasing q mitigates the noise in the image.

The POCS algorithm achieves the most improvement when χ is relatively large and η is small, unlike RSR. In that range, it is competitive with the RSR algorithm, but the improvement at smaller χ and larger η is quite a bit less than RSR. Neither the spectral angle nor the brightness error are noticeably different as a function of χ between the $q = 1$ and $q = 0.5$ settings. However, at $\eta < 0.6$, the $q = 0.5$ setting performs better on both metrics. When the isolation, η , is smaller, more measurements contribute to each pixel. Lowering q then puts stronger constraints on the uncoupling, which seems to lead to more information being reconstructed.

The POCS algorithm operated much more quickly on the simulated data than the RSR algorithm, achieving most of the improvement in the first few seconds (figure 15). It is possible

TABLE I
SUPER-RESOLUTION ACCURACY (AFTER 6 MIN)

Metric (means)	Reg.	RSR ₁₁	RSR ₂₁	RSR ₁₂	RSR ₂₂	RSR _{color}	POCS ₁	POCS _{0.5}
Spectral angle change (%)	0.00	1.27	-4.76	-1.65	-9.10	-8.02	-2.56	-3.49
Δ brightness change (%)	0.00	-1.93	-7.25	-1.37	-7.46	-7.08	-3.05	-4.08

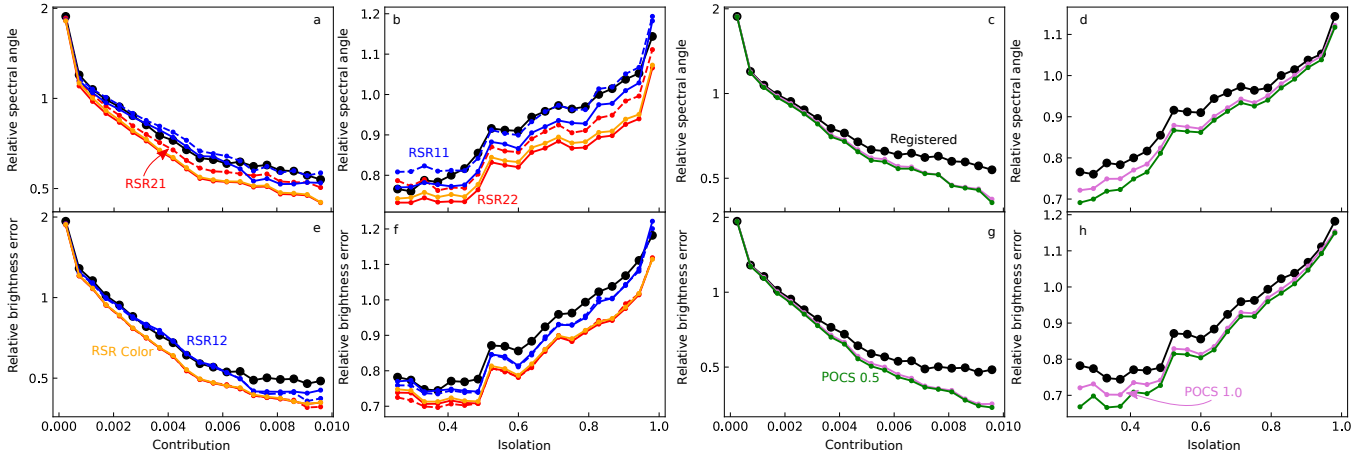


Fig. 11. The spectral angle (a-d) and brightness error (e-h) relative to the mean value of the registered image as a function of either contribution or isolation (equations 7 and 8), for both RSR and POCS.

that RSR could reach similar speeds by using new algorithms to evaluate the L_2 -norm [20]. Interestingly, the RSR methods that rely on L_1 -norm data consistency become worse after about 150 seconds. All the other algorithms show monotonic improvement in the metrics. The RSR algorithm with the color cost function shows less improvement than the L_2 -norm without it primarily because it is much slower. If there were a way to increase its speed, it would be at least comparable. In addition, the element-wise nature of POCS implies that it

might not scale well with the size of the images, and may be much less efficient for a large data cube.

VI. CONCLUSIONS

Our work here paves the way to the broader use of super-resolution in small mobile ocean observation platforms. Most importantly, it shows that super-resolution on ocean scenes can improve the accuracy of remote ocean observations. Moreover, super-resolution can be applied without disturbing the spectral

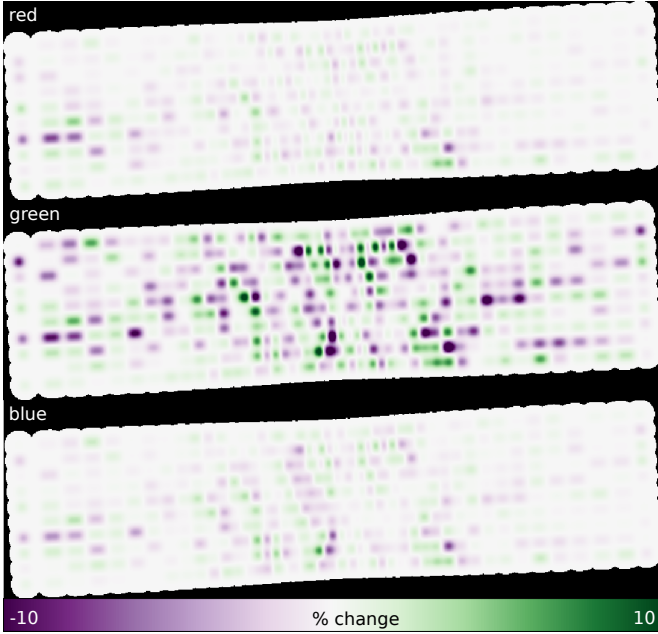


Fig. 12. The change from the registered image in the red, green, and blue channels from the POCS algorithm with $q = 1$.

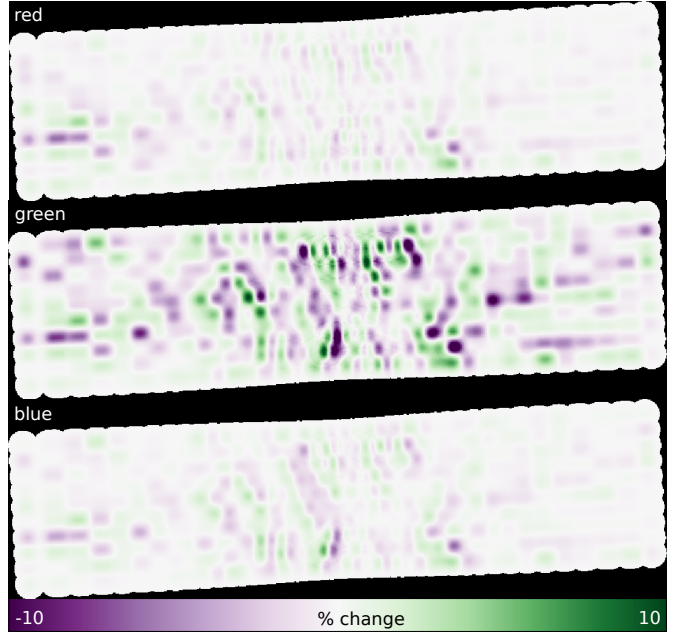


Fig. 13. The change from the registered image in the red, green, and blue channels from the POCS algorithm with $q = 0.5$.

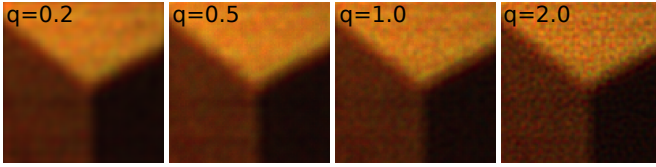


Fig. 14. Images of the wood block after being processed by POCS with varying q . Note how a smaller q mitigates coupling to noise.

integrity of the image, which is critical for hyperspectral data. However, the above experiments also point to several sets of questions that must be answered before it can be reliably incorporated into a data processing pipeline.

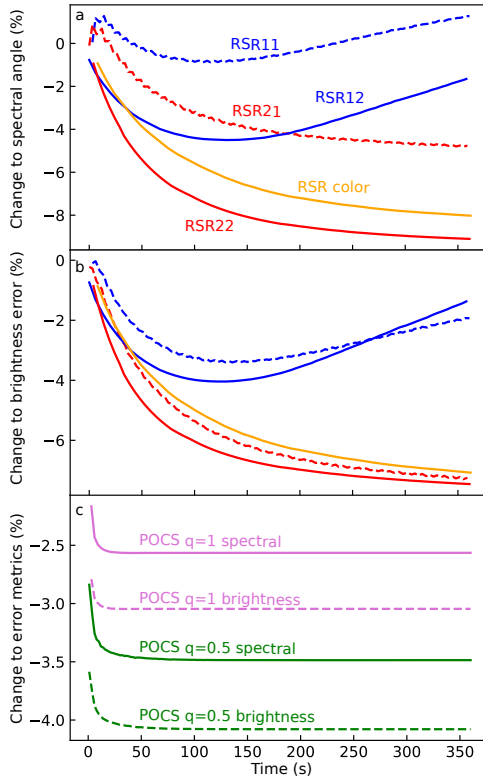


Fig. 15. The change in spectral angle (a) and brightness error (b) as a function of time for RSR. The change in both error metrics for POCS (c).

The first set of questions posed by the simulation relate to uncertainty. For images captured with an ordinary digital camera, the noise at any one pixel can be modelled reasonably well as being independent from any others. However, because super-resolution, particularly POCS, uses couplings between the footprints of neighboring measurements as a source of additional spatial information, the uncertainty becomes coupled between groups of pixels. The coupled nature of the uncertainty in super-resolution has the potential to implicitly bias data if it is not well understood. In addition, the types of hypotheses that are to be tested in ocean science typically relate to questions that are more complicated than the brightness of a pixel. If super-resolution reconstructions are to be used in ocean science it is critical to find a clear way to discuss uncertainty and to propagate it through the testing of a realistic hypothesis. Furthermore, super-resolution is designed

to improve spatial resolution, but quantifying the improvement is not yet a well-understood problem.

Because super-resolution relies on knowledge about either the scene or the imager, errors in either will harm reconstructions. The poor performance of the RSR algorithm with L_1 -norm smoothness on the ocean scene shows how incorrect knowledge can perform worse than no knowledge. The L_1 -norm works well on human-scale scenes [8], but the statistics of remote sensing images are different. What norm best describes ocean scenes? Can the reconstruction be constrained using knowledge of fluid dynamics [21], [22]? It is also critical to understand how uncertainty can be incorporated into the description of the imaging process. A cubesat will almost certainly not follow a trajectory as smooth as the one in the simulation. Some progress has been made to incorporate the uncertainty of a camera trajectory for multiframe super-resolution [23]. Both of these sources of uncertainty must be represented to the user in some form. A mathematical language to discuss them must be developed.

There are a few routes that would make super-resolution more feasible from a technical standpoint. First, the speed of super-resolution must be increased. A 10-second delay, much less a 360-delay, is far too long if super-resolution is to be integrated into robotic agents. Moreover, the preliminary tests shown here use RGB images, which have only three bands. Hyperspectral images have on the order of 100 bands, which will vastly slow down the algorithms if the extra bands are not dealt with carefully. Although the algorithms presented here are not fully optimized for speed, the observation that it took so long to reconstruct an image from merely 500 observations indicates that there may be difficulties utilizing super-resolution embedded devices, although several algorithms report faster speeds [8], [20], [24]. Second, if super-resolution could be interfaced with other analysis, compression or detection for example, more benefits of super-resolution may be uncovered.

The HICO™ image used for this study was provided by the Naval Research Laboratory, USA, and the Oregon State University through the NASA Ocean Color website [25]. NumPy, SciPy, and Matplotlib were used for the creation of code and figures [26]. JLG acknowledges funding from the European Research Council on Informatics and Mathematics postdoctoral fellowship. Funding for this work was provided by the Research Council of Norway (RCN) through the MASSIVE project, grant number 270959.

REFERENCES

- [1] D. M. Anderson, W. H. Ma, P. Andersen, V. M. Bricelj, J. J. Cullen, and J. E. J. Rensel, "Monitoring and Management Strategies for Harmful Algal Blooms in Coastal Waters," Asia Pacific Economic Program, Tech. Rep. APEC #201-MR-01.1, 2001.
- [2] J. Fortuna, F. Ferreira, R. Gomes, S. Ferreira, and J. Sousa, "Using low cost open source UAVs for marine wild life monitoring - Field Report*," *IFAC Proceedings Volumes*, vol. 46, no. 30, pp. 291–295, 2013. [Online]. Available: <https://linkinghub.elsevier.com/retrieve/pii/S1474667015403088>
- [3] Committee on Achieving Science Goals with CubeSats, Space Studies Board, Division on Engineering and Physical Sciences, and National Academies of Sciences, Engineering, and Medicine, *Achieving Science with CubeSats: Thinking Inside the Box*. Washington, D.C.: National Academies Press, Oct. 2016. [Online]. Available: <https://www.nap.edu/catalog/23503>

- [4] J. M. Bioucas-Dias, A. Plaza, G. Camps-Valls, P. Scheunders, N. Nasrabadi, and J. Chanussot, "Hyperspectral Remote Sensing Data Analysis and Future Challenges," *IEEE Geoscience and Remote Sensing Magazine*, vol. 1, no. 2, pp. 6–36, Jun. 2013. [Online]. Available: <http://ieeexplore.ieee.org/document/6555921/>
- [5] F. Sigernes, M. Syrjäsu, R. Storvold, J. Fortuna, M. E. Grøtte, and T. A. Johansen, "Do it yourself hyperspectral imager for handheld to airborne operations," *Optics Express*, vol. 26, no. 5, p. 6021, Mar. 2018. [Online]. Available: <https://www.osapublishing.org/abstract.cfm?URI=oe-26-5-6021>
- [6] S. C. Park, M. K. Park, and M. G. Kang, "Super-resolution image reconstruction: a technical overview," *IEEE Signal Processing Magazine*, vol. 20, no. 3, pp. 21–36, May 2003.
- [7] K. Nasrollahi and T. B. Moeslund, "Super-resolution: a comprehensive survey," *Machine Vision and Applications*, vol. 25, no. 6, pp. 1423–1468, Aug. 2014. [Online]. Available: <http://link.springer.com/10.1007/s00138-014-0623-4>
- [8] S. Farsiu, M. Robinson, M. Elad, and P. Milanfar, "Fast and Robust Multiframe Super Resolution," *IEEE Transactions on Image Processing*, vol. 13, no. 10, pp. 1327–1344, Oct. 2004. [Online]. Available: <http://ieeexplore.ieee.org/document/1331445/>
- [9] H. Stark and P. Oskoui, "High-resolution image recovery from image-plane arrays, using convex projections," *Journal of the Optical Society of America A*, vol. 6, no. 11, p. 1715, Nov. 1989. [Online]. Available: <https://www.osapublishing.org/abstract.cfm?URI=josaa-6-11-1715>
- [10] N. Efrat, D. Glasner, A. Apartsin, B. Nadler, and A. Levin, "Accurate Blur Models vs. Image Priors in Single Image Super-resolution," in *2013 IEEE International Conference on Computer Vision*. Sydney, Australia: IEEE, Dec. 2013, pp. 2832–2839. [Online]. Available: <http://ieeexplore.ieee.org/document/6751463/>
- [11] J. Bechhoefer, "What is superresolution microscopy?" *American Journal of Physics*, vol. 83, no. 1, pp. 22–29, Jan. 2015. [Online]. Available: <http://aapt.scitation.org/doi/10.1119/1.4900756>
- [12] R. L. Lucke, M. Corson, N. R. McGlothlin, S. D. Butcher, D. L. Wood, D. R. Korwan, R. R. Li, W. A. Snyder, C. O. Davis, and D. T. Chen, "Hyperspectral Imager for the Coastal Ocean: instrument description and first images," *Applied Optics*, vol. 50, no. 11, p. 1501, Apr. 2011. [Online]. Available: <https://www.osapublishing.org/abstract.cfm?URI=ao-50-11-1501>
- [13] E. Ringaby, O. Friman, P.-E. Forssen, T. O. Opsahl, T. V. Haavardsholm, and I. Kasen, "Anisotropic Scattered Data Interpolation for Pushbroom Image Rectification," *IEEE Transactions on Image Processing*, vol. 23, no. 5, pp. 2302–2314, May 2014. [Online]. Available: <http://ieeexplore.ieee.org/document/6786301/>
- [14] H. E. Torkildsen and T. Skauli, "Full characterization of spatial coregistration errors and spatial resolution in spectral imagers," *Optics Letters*, vol. 43, no. 16, p. 3814, Aug. 2018. [Online]. Available: <https://www.osapublishing.org/abstract.cfm?URI=ol-43-16-3814>
- [15] S. Riazanoff, "SPOT 123-4-5 Geometry Handbook," GAEL Consultant, Champs-sur-Marne, France, Tech Rep. GAEL-P135-DOC-001, 2004.
- [16] M. Irani and S. Peleg, "Improving resolution by image registration," *CVGIP: Graphical Models and Image Processing*, vol. 53, no. 3, pp. 231–239, May 1991. [Online]. Available: <http://linkinghub.elsevier.com/retrieve/pii/104996529190045L>
- [17] A. M. Tekalp, M. K. Ozkan, and M. I. Sezan, "High-resolution image reconstruction from lower-resolution image sequences and space-varying image restoration," in *[Proceedings] ICASSP-92: 1992 IEEE International Conference on Acoustics, Speech, and Signal Processing*, vol. 3, Mar. 1992, pp. 169–172 vol.3.
- [18] A. Patti, M. Sezan, and A. Murat Tekalp, "Superresolution video reconstruction with arbitrary sampling lattices and nonzero aperture time," *IEEE Transactions on Image Processing*, vol. 6, no. 8, pp. 1064–1076, Aug. 1997. [Online]. Available: <http://ieeexplore.ieee.org/document/605404/>
- [19] S. Farsiu, M. Elad, and P. Milanfar, "Multiframe demosaicing and super-resolution of color images," *IEEE Transactions on Image Processing*, vol. 15, no. 1, pp. 141–159, Jan. 2006. [Online]. Available: <http://ieeexplore.ieee.org/lpdocs/epic03/wrapper.htm?arnumber=1556633>
- [20] N. Zhao, Q. Wei, A. Basarab, N. Dobigeon, D. Kouame, and J.-Y. Tourneret, "Fast Single Image Super-Resolution Using a New Analytical Solution for L₂ – L₂ Problems," *IEEE Transactions on Image Processing*, vol. 25, no. 8, pp. 3683–3697, Aug. 2016. [Online]. Available: <http://ieeexplore.ieee.org/document/7468504/>
- [21] P. Ruhnau, A. Stahl, and C. Schnörr, "Variational estimation of experimental fluid flows with physics-based spatio-temporal regularization," *Measurement Science and Technology*, vol. 18, no. 3, pp. 755–763, Mar. 2007. [Online]. Available: <http://stacks.iop.org/0957-0233/18/i=3/a=027?key=crossref.fd703ab7182ec4df1443b1b7add75d1b>
- [22] J. Gregson, I. Ihrke, N. Thuerey, and W. Heidrich, "From capture to simulation: connecting forward and inverse problems in fluids," *ACM Transactions on Graphics*, vol. 33, no. 4, pp. 1–11, Jul. 2014. [Online]. Available: <http://dl.acm.org/citation.cfm?doid=2601097.2601147>
- [23] S. D. Babacan, R. Molina, and A. K. Katsaggelos, "Variational Bayesian Super Resolution," *IEEE Transactions on Image Processing*, vol. 20, no. 4, pp. 984–999, Apr. 2011. [Online]. Available: <http://ieeexplore.ieee.org/document/5585756/>
- [24] J. Johnson, A. Alahi, and L. Fei-Fei, "Perceptual Losses for Real-Time Style Transfer and Super-Resolution," in *Computer Vision – ECCV 2016*, B. Leibe, J. Matas, N. Sebe, and M. Welling, Eds. Cham: Springer International Publishing, 2016, vol. 9906, pp. 694–711. [Online]. Available: http://link.springer.com/10.1007/978-3-319-46475-6_43
- [25] NASA Goddard Space Flight Center, Ocean Ecology Laboratory, Ocean Biology Processing Group, "Hyperspectral Imager for the Coastal Ocean (HICO) Ocean Color Data." [Online]. Available: <https://oceancolor.gsfc.nasa.gov/data/hico/>
- [26] F. Perez, B. E. Granger, and J. D. Hunter, "Python: An Ecosystem for Scientific Computing," *Computing in Science & Engineering*, vol. 13, no. 2, pp. 13–21, Mar. 2011. [Online]. Available: <http://ieeexplore.ieee.org/document/5582063/>